Supporting Information

Controllable Synthesis of Porous Tubular Carbon with a Ag+-ligand Assisted Stöber-Silica/Carbon Assembly Process

Yang-Lin Shen,[a] Jun-Ling Jin,[b] Ning Chen,[a] Peng Ju Li,[a] Ting Xu,[a] Yun-Peng Xie*[a] and Xing Lu*[a]
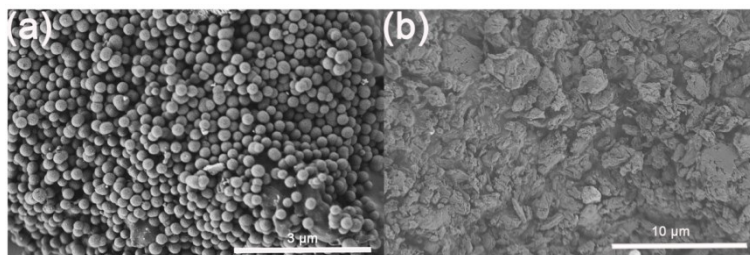
Fig. S1. SEM images of silica/RF hybrid synthesized with 0 mmol (a) and 0.15 mmol Ag+ (b).
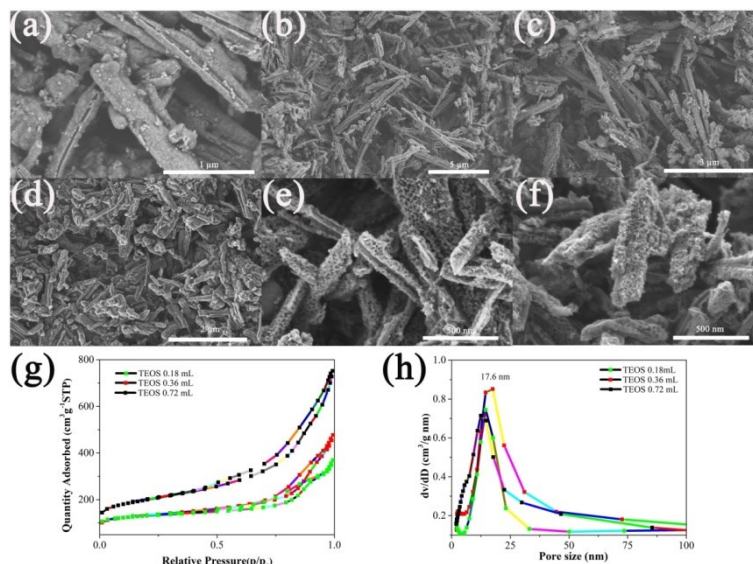

Fig. S2. SEM images of as-synthesized silica/RF hybrids via Ag-PFS assisted SSCA with different amount of TEOS: (a) 0.18 mL; (b) 0.36 mL; (c) 0.72 mL. SEM images of carbon obtained by these silica/RF hybrids after carbonization and silica removal: (d) 0.18 mL; (e) 0.36 mL; (f) 0.72 mL. BET measurement of N_2 adsorption/desorption isotherms (g) and pore size distribution (f) of these tubular carbon samples.

Table S1. BET results summary of these tubular carbon obtained in a different amount of TEOS.

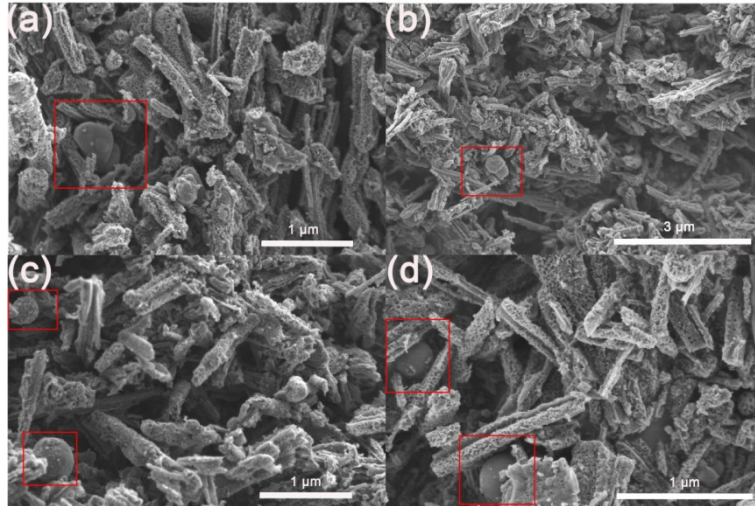| TEOS (mL)	BET SSA (m^2g^{-1})	Pore volume (m^3g^{-1})	Pore size (nm)
0.18	445	0.49	14.3
0.36	452	0.64	17.6
0.72	696	1.04	12.6

Fig. S3. The morphologies of the synthesized porous carbon mixed with carbon spheres (red frame).
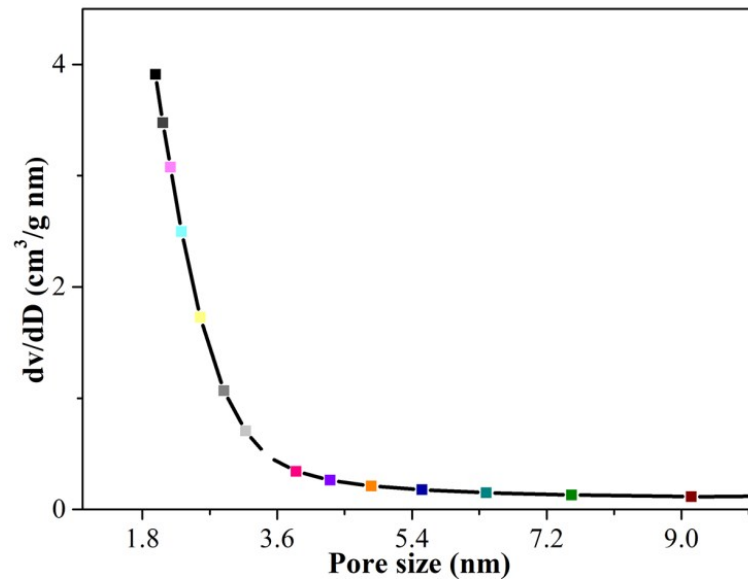

Fig. S4. The pore size distribution of **RF2** synthesized with 0.1 ml EDA.
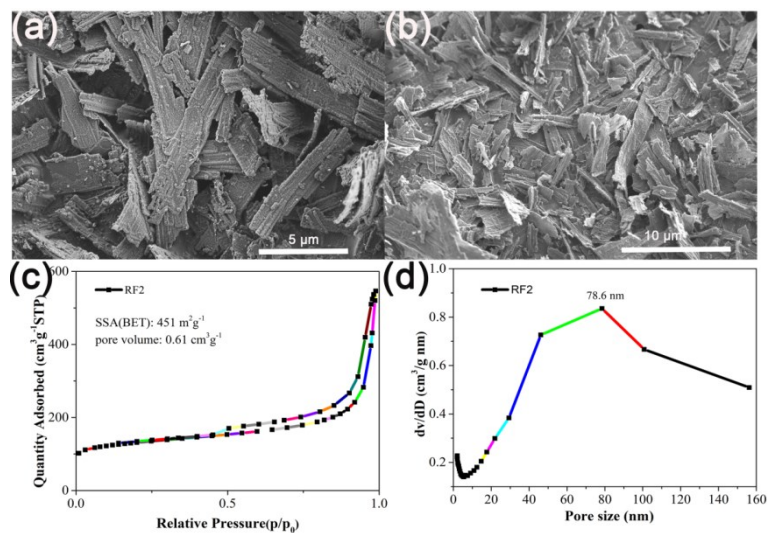
Fig. S5. (a) and (b) The as-synthesized silica/RF hybrid and tubular carbon **RF2** with 0.5 ml EDA; (c) and (d) BET measurement of N_2 adsorption/desorption isotherms and pore size distribution of the porous tubular carbon, respectively.
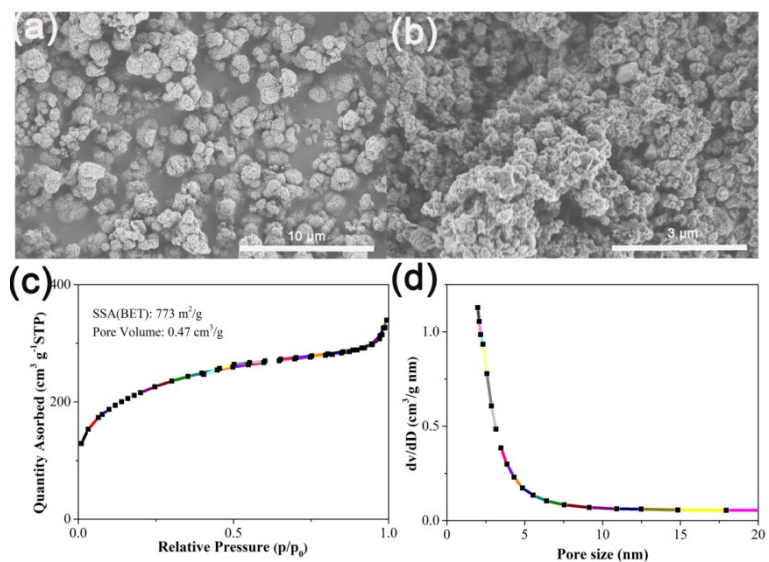

Fig. S6. (a) and (b) The as-synthesized silica/polydopamine hybrid and carbon via SSCA without silver; (c) and (d) BET measurement of N_2 adsorption/desorption isotherms and pore size distribution of the porous tubular carbon, respectively.
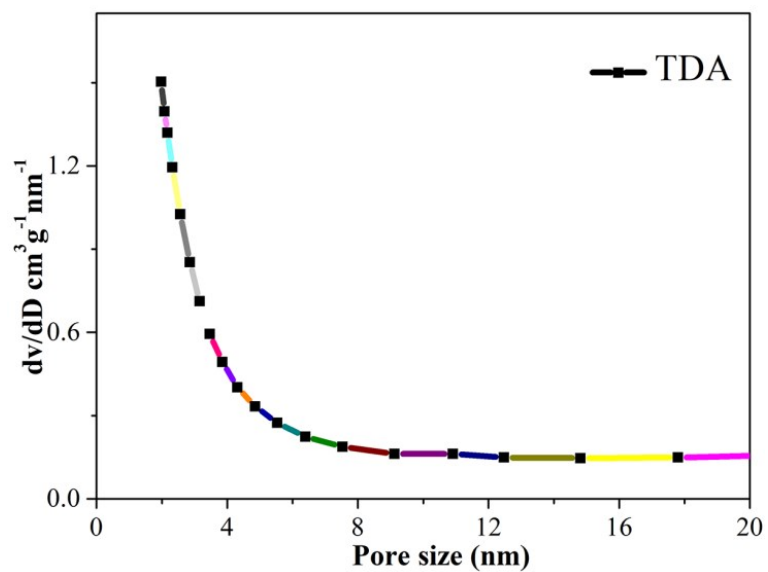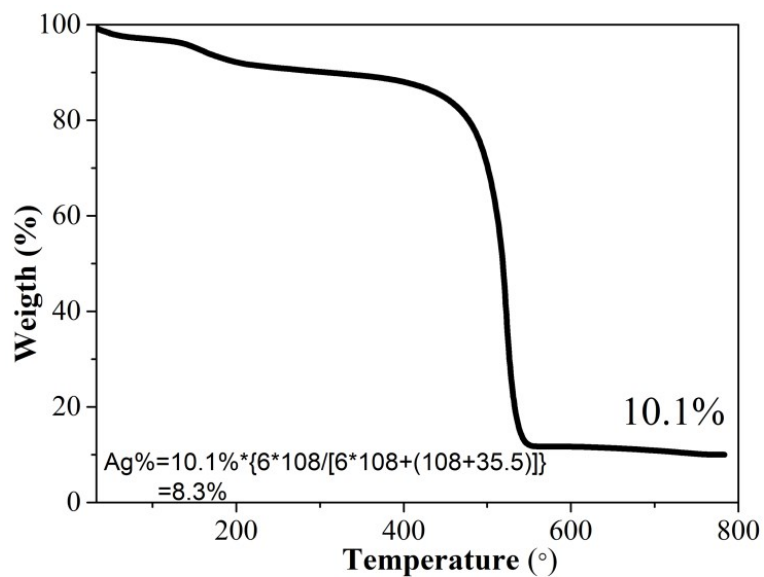
Fig. S7. The pore size distribution of **TDA**.

$$Ag\% = 10.1\% * \{6*108/[6*108+(108+35.5)]\} = 8.3\%$$

10.1%

Fig. S8. Thermal gravimetric analysis of **TDA** and the loading of metal silver determined in combination with XPS results.

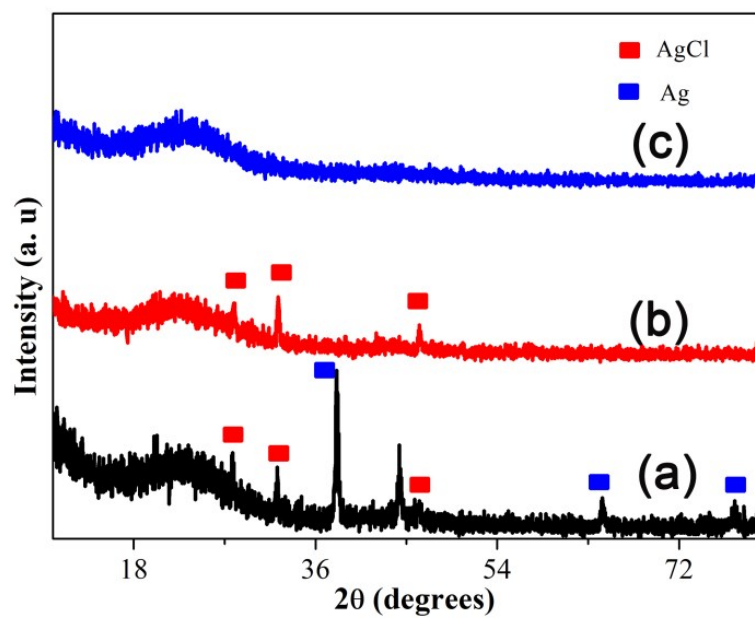**Fig. S9.** (a) XRD patterns of **TDA**; (b) **TDA** after 2 M HNO_3 treatment; (c) **TDA** after 2 M HNO_3 and KSCN treatment.
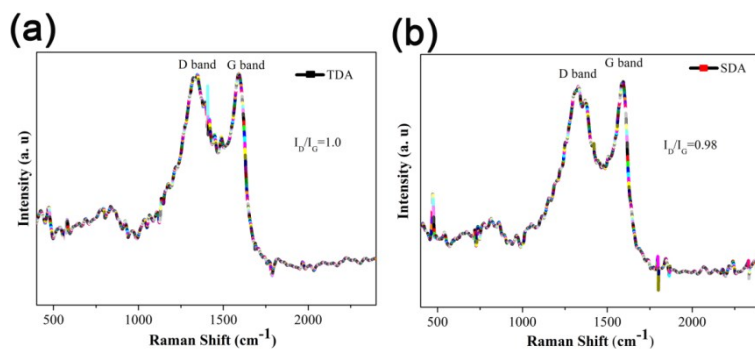

Fig. S10. Raman spectrums of **TDA** (a) and **SDA** (b).

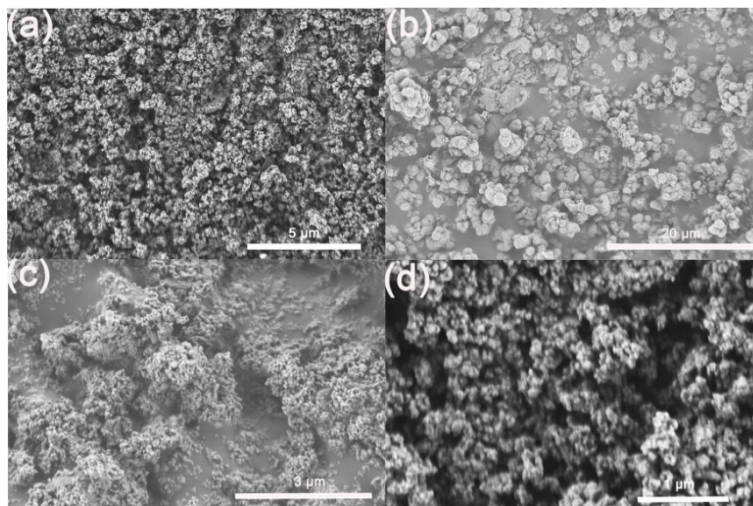**Fig. S11.** The as-synthesized silica/DA hybrid via SSCA with $Co(NO_3)_2$ (a), $Pt(NO_3)_2$ (b), $SnCl_2$ (c) and $FeCl_3$ (d).
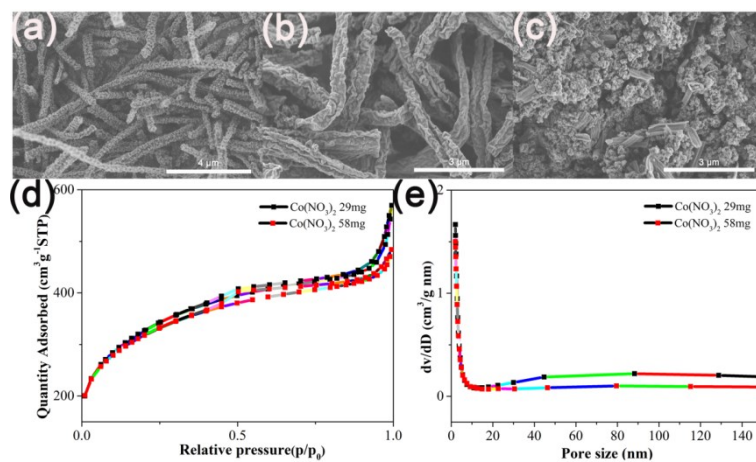

Fig. S12. The porous carbon synthesized by SSCA with silver-PFS and different amounts of $Co(NO_3)_2$ $6H_2O$. (a) 29 mg (0.1 mmol); (b) 58 mg (0.2mmol); (c) 116 mg (0.4 mol); (d) and (e) BET measurement of N_2 adsorption/desorption isotherms and pore size distribution of the porous tubular carbon, respectively.

Table S2. BET results summary of the carbon obtained in a different amount of $Co(NO_3)_2$ $6H_2O$

$Co(NO_3)_2$ (mg)	BET SSA (m^2g^{-1})	Pore volume (m^3g^{-1})	Pore size (nm)
29	1170	0.76	< 2
58	1129	0.69	< 2
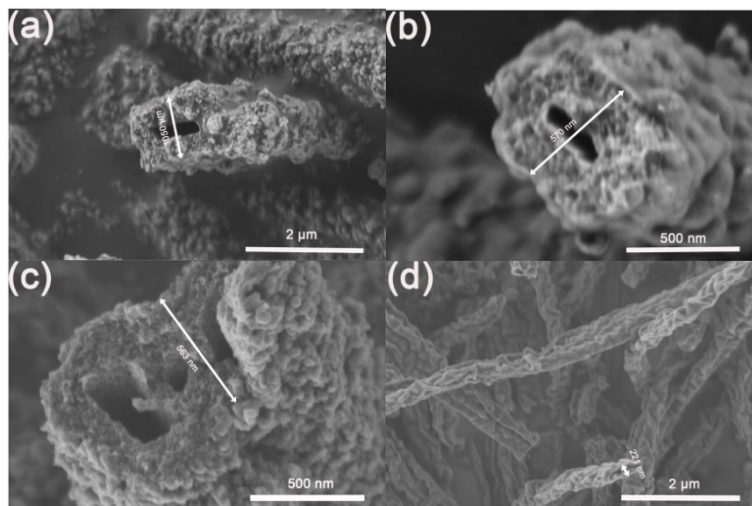
Fig. S13. (a) and (c) The as-synthesized silica/polydopamine hybrid and TDA carbon with 0mg Co(NO$_3$)$_2$ 6H$_2$O; (b) and (d) The as-synthesized silica/polydopamine hybrid and TDA carbon with 58mg Co(NO$_3$)$_2$ 6H$_2$O.
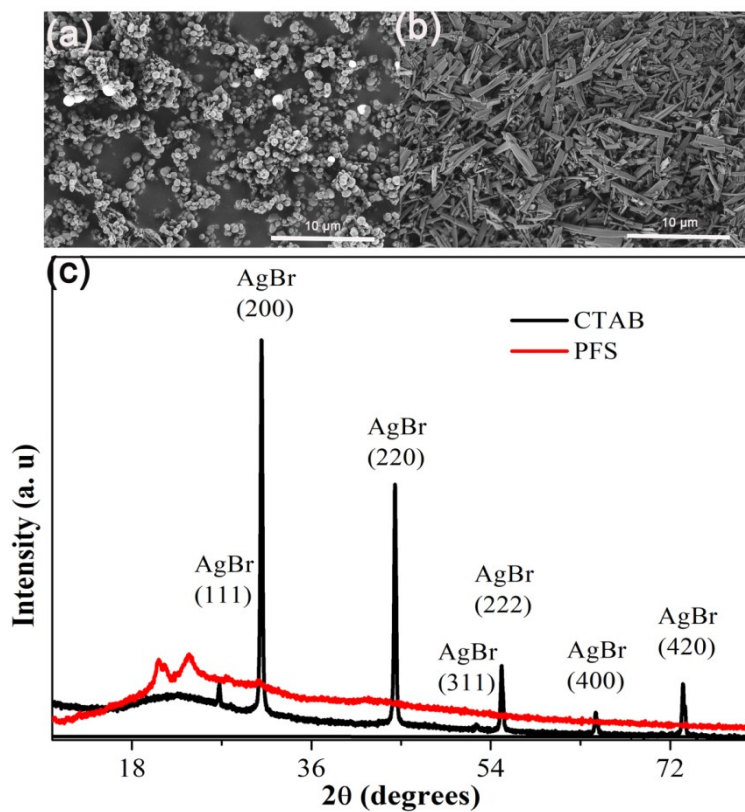

Fig. S14. SEM images and XRD pattern of silica synthesized by CTAB (a) and PFS (b).
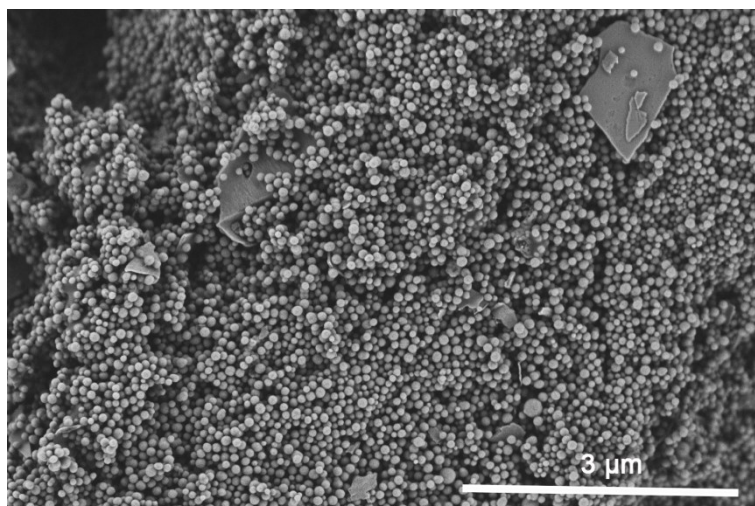
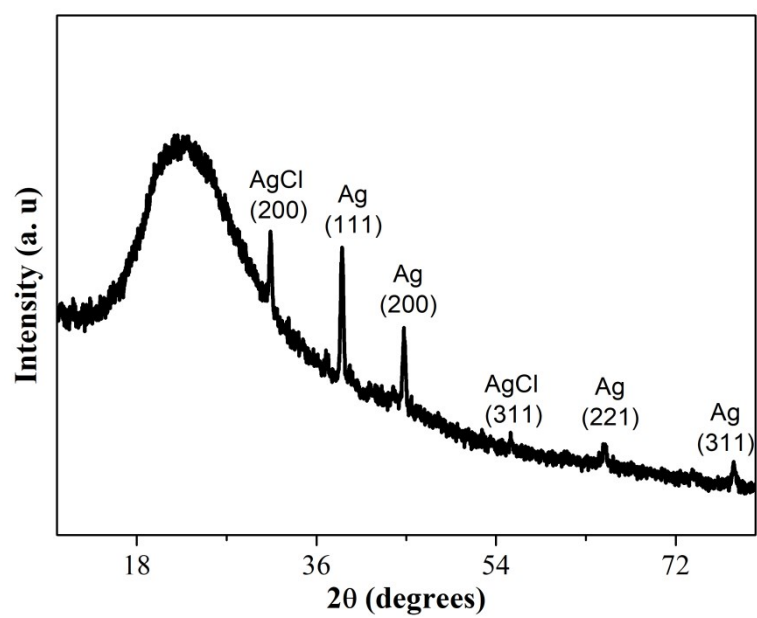**Fig. S15.** SEM image of silica synthesized by PFS·PF$_6$.

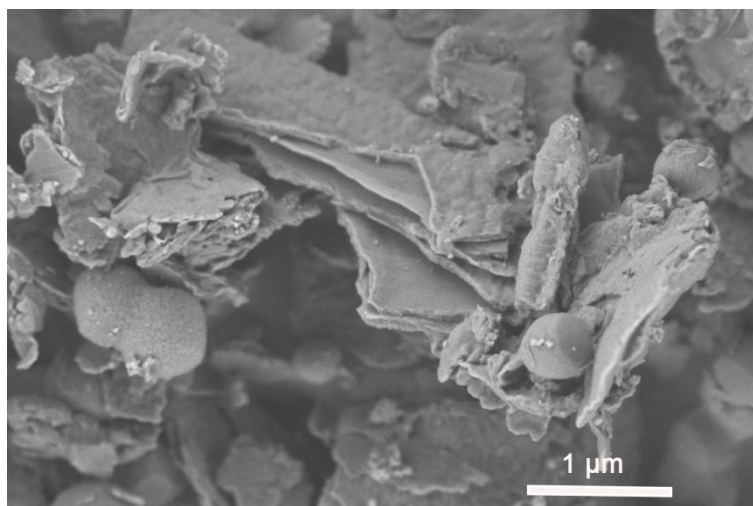**Fig. S16.** XRD pattern of as-synthesized silica/dopamine hybrid.

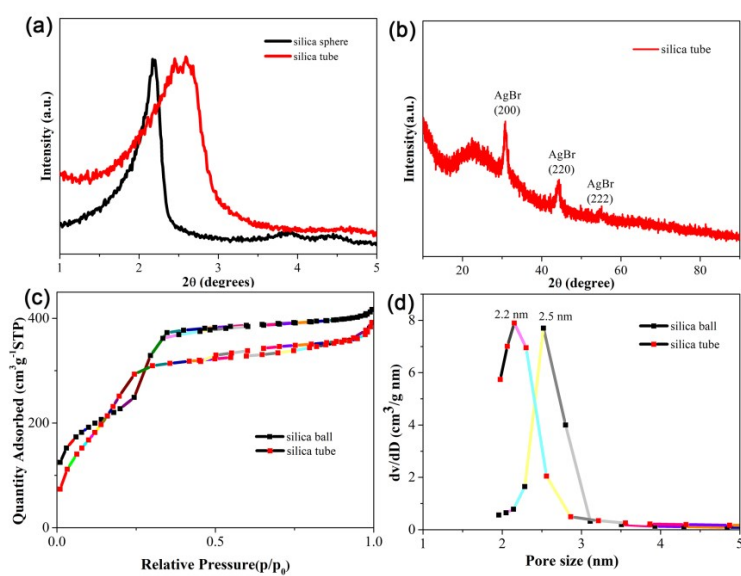**Fig. S17.** SEM image of silica synthesized by 10ml ammonia.

Fig. S18. XRD patterns and N_2 adsorption-desorption isotherms of silica sphere and tube synthesized with and without silver after calcination.
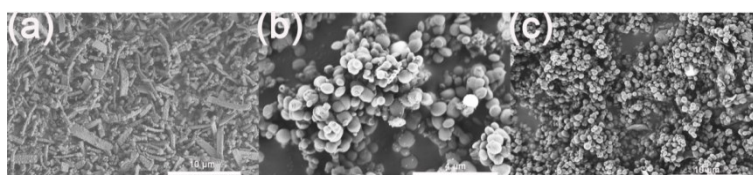

Fig. S19. SEM images of as-synthesized silica with different amount of silver: (a) 0.05 mmol; (b) 0.2 mmol; (c) 0.4 mmol.
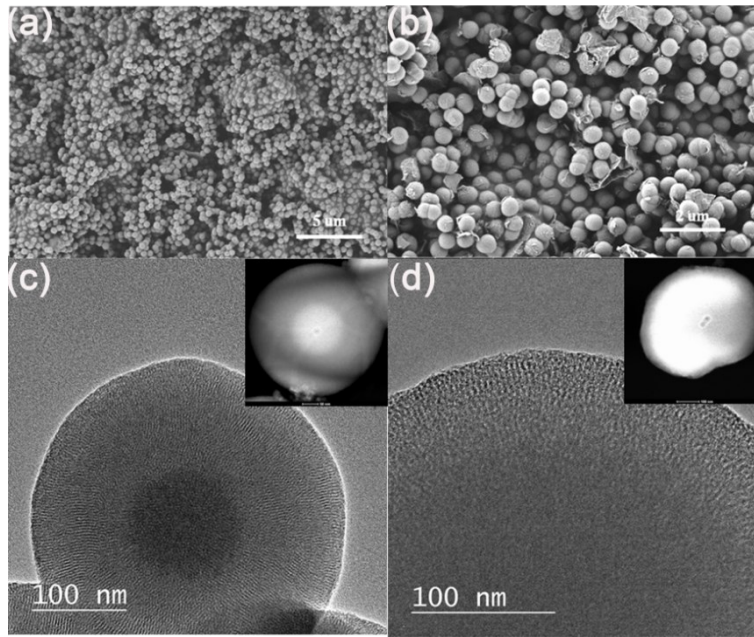
Fig. S20. The characterization of silica balls synthesized by the Zn and Cu ion-assisted method. (a) SEM image of Zn-silica-sphere; (b) SEM image of Cu-silica-sphere; (c) TEM and STEM images of Zn-silica-sphere; (d) TEM and STEM images of Cu-silica-sphere.
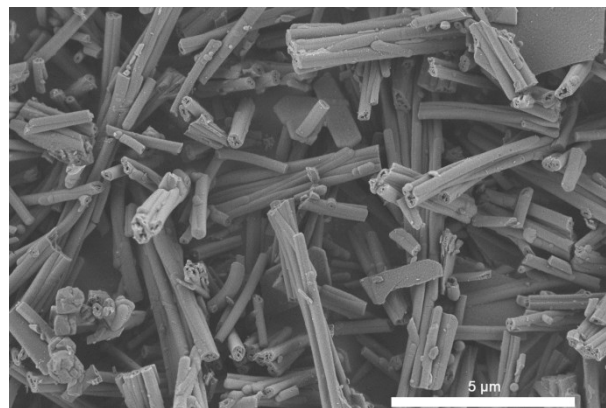

Fig. S21. SEM images of as-synthesized silica intermediates with silver and PFS surfactant.
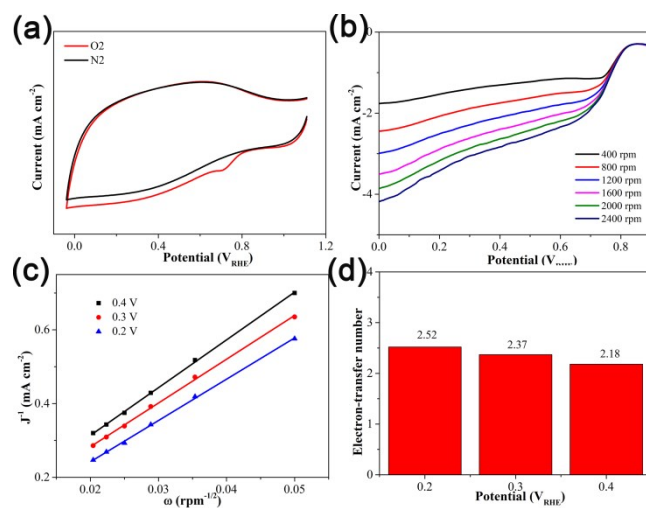
Fig. S22. The catalytic activity of the **SDA** towards the electrochemical reduction of oxygen in 0.1 M KOH electrolyte: (a) CV curves of **SDA** performed in O_2 and N_2 -saturated 0.1 M KOH electrolytes with a scan rate of 50 mV s^{-1}; (b) LSV curves of **SDA** at a scan rate of 10 mV s^{-1} with various rotation rates from 400 to 2400 rpm; (c) K-L plots derived from LSV curves of **SDA** at different electrode potentials. (d) electron-transfer number of **SDA** in ORR at 0.2V, 0.3V, and 0.4 V, respectively.
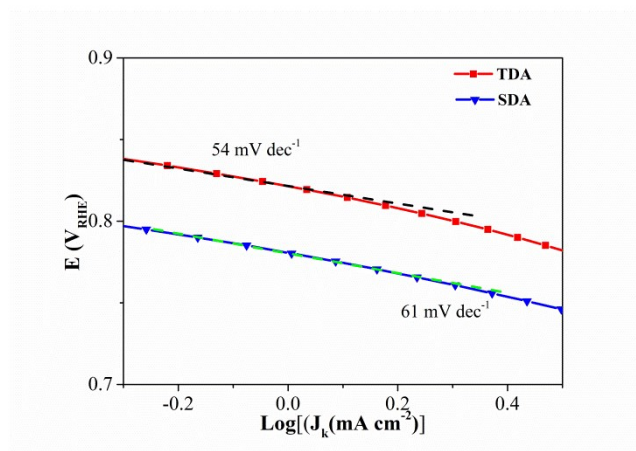

Fig. S23. The Tafel plot of **SDA** and **TDA** at 1600 rpm in O_2-saturated 0.1 M KOH.
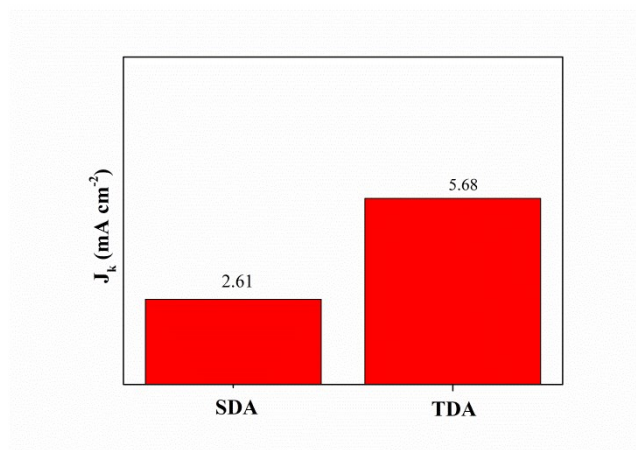
Fig. S24. Kinetic-limiting current density at -0.75 V of **SDA** and **TDA**. Rotating speed: 1600 rpm and scan rate: 10 mV s^{-1}.
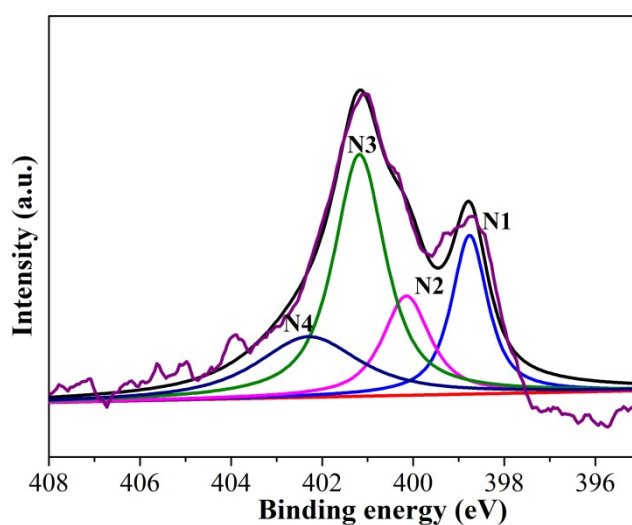

Fig. S25. Deconvoluted N 1s spectra of **SDA**.

Table. S3. The C and N content measured from elemental analysis and N dopant proportions of **SDA** and **TDA** catalysts measured from the fitting of the N 1s XPS.

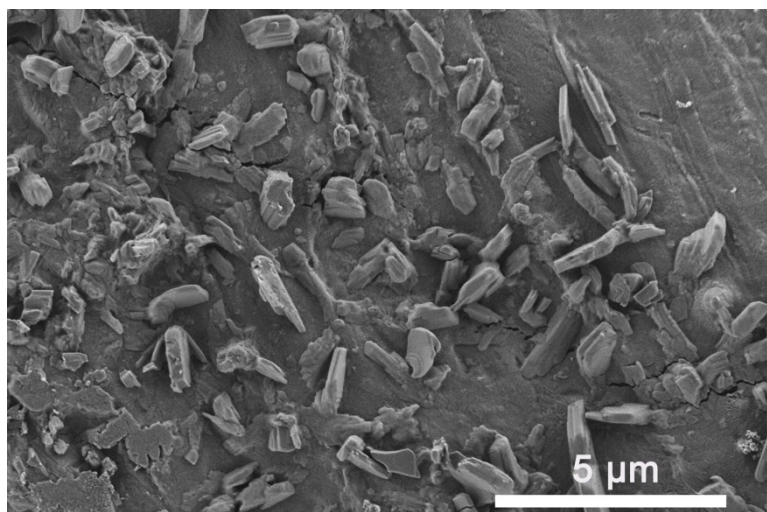| Sample | C /wt% | N /wt% | Relative content of different N species / 100% | | | | $N_{(pyridinic+graphitic)}$ /N_{total} |
			pyridinic-N (N1)	pyrrolic-N (N2)	graphitic-N (N3)	pyridine-N-oxide (N4)	
SDA	92.93	2.42	0.12	0.09	0.64	0.15	0.76
TDA	90.38	3.63	0.12	0.15	0.65	0.08	0.77

Fig. S26. SEM image of silica particles synthesized in the acid condition.
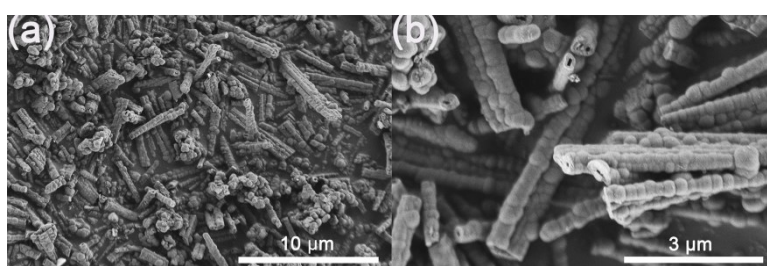

Fig. S27. SEM images of as-synthesized particles synthesized in the Stöber-silica/carbon co-assembly with 1 mmol Ni^{2+} and 0.1 mmol Ag^+.